

Spectral evolution of bottom-forced internal waves

J.A. MacKinnon and K.B. Winters

Scripps Institution of Oceanography, La Jolla, CA

Abstract.

Recent observations and analysis suggest that rough abyssal topography serves as a generation site for energetic internal waves. The elevated turbulence that these waves produce may be an important part of global circulation and energy budgets. We have conducted a series of idealized numerical experiments to investigate internal wave evolution and interaction above rough topography. The non-hydrostatic equations of motion are solved in a horizontally periodic, domain with free-slip top and bottom boundary conditions, allowing nonlinear interactions between about 105 wave modes. We do not explicitly consider the wave generation problem, but instead force each simulation with a narrowband, upwardly propagating internal tide as a (near) bottom boundary condition. Three simulations are run with varying amplitude at a low-latitude (26° S) chosen to match the Brazil Basin mixing experiment. For comparison, three simulations were also run at at mid-latitude (45° S).

In all cases nonlinear interactions quickly transfer energy to a wide range of scales and frequencies. Once a quasi-steady state is achieved, energy spectra are characterized by high-frequency slopes with close spectral slopes close to -2, in qualitative agreement with numerous observations and models. In contrast, vertical wavenumber spectra retain more of a narrowband signature, with deviations in shape that respond sensitively to changes in forcing amplitude. Two-dimensional spectra are non-separable in vertical wavenumber and frequency, with a band of energy at low-wavenumbers extending through all frequencies. The numerical predictions of turbulent dissipation appear to be realistically patchy in space and time with a strongly decreasing trend with height in all simulations. All simulations yield an approximately quadratic relationship between the average shear variance and the volume integrated dissipation rate.

There are two major distinctions between low- and mid-latitude results. First, at low-latitude, nonlinear interactions transfer energy from tidal to near-inertial waves, while at mid-latitude energy remains concentrated near the forcing frequency ($M2$) and wavenumber. At low-latitude, the frequency shift occurs within a few days of the initiation of forcing. Second, the average mid-latitude dissipation rate is larger than that at low-latitude for comparable wavefield energy, especially near the forcing region, qualitatively consistent with observations and theoretical predictions. We hypothesize that the dramatic difference in the rate of energy transfer out of the tidal band between the low- and mid-latitude experiments is loosely related to Parametric Subharmonic Instability (PSI) - an idealized type of wave-wave interaction possible only at low latitudes.

Introduction

The study of deep ocean mixing remains a vital and vibrant part of the quest to understand and model ocean circulation. Deep and abyssal mixing maintain the meridional gradients that drive the overturning circulation, determine average isopycnal locations, and control deep lateral circulation and upwelling. The order of magnitude discrepancy between the rate of turbulent diapycnal mixing inferred necessary to close global budgets and typical measurements has been a long-standing cause of concern in the small-scale oceanographic community. The relatively low magnitude of typical thermocline diffusivity ($\sim 5 \times 10^{-6} \text{m}^2 \text{s}^{-1}$) has been confirmed by both microstructure [Gregg 1998, Polzin et al

1995] and tracer release [Ledwell et al 1993] studies, and is consistent with several models of internal wave-wave interaction as governing dynamic [Henyey et al 1996, McComas and Muller 1981, Winters and D'Asaro 1997].

Recent observations in the Brazil Basin [Polzin et al 1997, Ledwell et al 2000] have strengthened earlier suspicions [Munk 1966] that much of the 'missing mixing' may be occurring over regions of rough topography. Polzin et al [1997] found diapycnal diffusivities well above $10^{-4} \text{m}^2 \text{s}^{-1}$ that extended (with declining magnitude) well above the highest topography. They suggested that the elevated turbulence is related to the presence of an energetic internal wave field generated locally by the interaction of the barotropic tide with rough topography. The implications of

such patterns of elevated mixing are global - *Simmons et al* [2003] and *Hasumi and Sugimoto* [1999] demonstrate that the structure and magnitude of deep circulation and upwelling sensitively respond to bottom-intensified, horizontally inhomogeneous diffusivity.

The internal-wave generation problem has received a surge of recent attention (e.g. *St. Laurent and Nash* [this issue], *Polzin* [this issue], *St Laurent and Garrett* [2002], *Llewellyn Smith and Young* [2002], and *Egbert and Ray* [2000]). Efficient generation is found to occur over a wide range of topography, from fracture zones to sea-mounts to island arcs to mid-ocean ridges. *St. Laurent and Nash* [this issue] argue that the lowest generated modes radiate away from the generation site, while higher modes are trapped locally. They hypothesize that nonlinear interactions in the vicinity of forcing regions transfer energy to dissipative scales, leading to observed patterns of elevated turbulence. The nature of such interactions, and sensitivity to the magnitude and spectral character of generated waves, is a major open question and is the subject of the work presented here.

We have undertaken a series of idealized numerical experiments to study internal wave energy transfers in energetic regions - in particular above sites of topographic internal wave generation. These experiments do not directly address wave generation, but impose an upward propagating internal wave field as a (near) bottom boundary condition, and explore the energy transfer rate, steady-state spectral properties, and the numerical analog to turbulent dissipation as functions of depth. Here we present results using spectrally localized wave forcing and consider the sensitivity of results to changes in forcing wave amplitude and latitude.

Numerical Methods

The numerical model used here is an updated version of the three-dimensional, pseudo-spectral non-hydrostatic code used by *Winters and D'Asaro* [1997], and is more fully described in *Winters et. al.* [2003]. Generally, this choice of model and associated parameters reflects our focus on interactions within the internal wave continuum rather than the details of wave generation or dissipation. Approximately 10^5 wave modes are free to interact via the inviscid Navier-Stokes equations. Energy transferred to scales smaller than about 1 km horizontally and 100 m vertically is removed through hyperviscosity. This removal rate, or equivalently the rate of downscale transport then serves as an estimate of the dissipation rate, ϵ .

Specifically, the model solves the equations of motion in an incompressible, rotating ocean with arbitrary forcing,

$$\frac{\partial u}{\partial t} = -\vec{u} \cdot \nabla u + fv - \frac{1}{\rho_0} \frac{\partial p'}{\partial x} + \nu_{\mathbf{p}} \cdot \nabla^p u + F_u$$

$$\begin{aligned} \frac{\partial v}{\partial t} &= -\vec{u} \cdot \nabla v - fu - \frac{1}{\rho_0} \frac{\partial p'}{\partial y} + \nu_{\mathbf{p}} \cdot \nabla^p v + F_v \\ \frac{\partial w}{\partial t} &= -\vec{u} \cdot \nabla w - \frac{1}{\rho_0} \frac{\partial p'}{\partial z} - \frac{g\rho'}{\rho_0} + \nu_{\mathbf{p}} \cdot \nabla^p w + F_w \\ \frac{\partial \rho'}{\partial t} &= -\vec{u} \cdot \nabla \rho' - w \frac{\partial \bar{\rho}}{\partial z} + \kappa_{\mathbf{p}} \cdot \nabla^p \rho' + \kappa \frac{\partial^2 \bar{\rho}}{\partial z^2} + F_{\rho'} \\ \nabla \cdot \vec{u} &= 0, \end{aligned} \quad (1)$$

where (u, v, w) is the velocity vector, ρ' is the density perturbation from a linearly increasing average density profile ($\bar{\rho}$), p' is the perturbation pressure, ρ_0 is a reference density, and f is the inertial frequency. The model is solved in a rectangular domain of size (L_x, L_y, L_z) with (n_x, n_y, n_z) evenly spaced grid points, horizontally periodic boundary conditions and free-slip top and bottom boundary conditions (Table 1). It must be justified a posteriori that the available bandwidth is enough to capture the important interaction scales. To address this question, we varied the resolution for one case and found that the major features discussed here (spectral slopes and average dissipation rates) did not substantially change with increased resolution.

The coefficients ($\nu_{\mathbf{p}}$, $\kappa_{\mathbf{p}}$) and exponent (p) of the hyperviscosity terms in (1) are chosen to maximize the range of inviscid wavenumbers while removing energy from the smallest resolved scales quickly enough to maintain numerical stability. Based upon these equations we define a ‘hyper-dissipation’ rate (henceforth simply referred to as the dissipation rate),

$$\epsilon = \nu_{p,j} \left[\frac{\partial}{\partial x_j} u_{kk} \right]^2 \quad (2)$$

that describes the rate at which energy is transferred to dissipative scales by inviscid dynamics.

The simulations are initialized at rest and forced with a bottom-localized, narrowband field of upward-propagating internal waves of tidal(M2) frequency, a modification of the forcing used by *Slinn and Riley* [1998]. For example, forcing of vertical velocity is specified as the time derivative of a hypothesized forcing wave velocity,

$$F_w = \frac{\partial w_F}{\partial t} = \sum_{\mathbf{k}} -A_{\mathbf{k}} \omega_0^2 e^{i[\mathbf{k} \cdot \mathbf{x} - \omega_0 t]} F(z) \quad (3)$$

$$\mathbf{k} = [k_x, k_y, k_z(k_x, k_y, \omega_0)] \quad (4)$$

$$F(z) = e^{-b^2 z^2}. \quad (5)$$

The simulations presented here were forced with a narrow gaussian distribution of spectral amplitudes ($A_{\mathbf{k}}$) around a central horizontal wavenumber,

$$A_{\mathbf{k}} = A_0 e^{-\left[\frac{k_x - k_{x0}}{\beta}\right]^2 - \left[\frac{k_y - k_{y0}}{\beta}\right]^2}, \quad (6)$$

where A_0 physically represents a typical vertical displacement. The central horizontal wavevector (k_{x0}, k_{y0}) is oriented eastward in these f-plane simulations without loss of

Table 1. Parameters common to all runs

L_x	50 km	n_x	128	k_{x0}	$6.3 \times 10^{-4} \text{ m}^{-1}$	N	$2 \times 10^{-3} \text{ s}^{-1}$
L_y	50 km	n_y	64	k_{y0}	0 m^{-1}	ω_0	$1.4 \times 10^{-4} \text{ s}^{-1}$
L_z	5 km	n_z	128				

generality (Table 1). For each pair of horizontal wavenumbers (k_x, k_y) , the vertical wavenumber is calculated from the dispersion relationship for a given forcing frequency, ω_0 . The characteristic scale (b) of the vertical localization function (F) is chosen to allow at least one full vertical wavelength in the forcing region ($b = 1.5k_{z0}$).

The results from six runs are presented here (Table 2), three each at low-latitude (LL) and mid-latitude (ML). Runs LL1 and ML1 are presented in some detail; they have the same forcing amplitude, but have different local inertial frequencies, representing low (26 S) and mid-latitude (45 S) environments. The low latitude value was chosen to match that of the Brazil Basin observations. The central forcing wavenumber k_0 and wave amplitude A_0 were chosen to approximately match the magnitude and characteristic horizontal wavenumber of the peak upward energy flux calculated by *St. Laurent and Garrett* [2002]. Note that as latitude changes, so does the vertical wavenumber of the forcing waves, which is set by the chosen horizontal wavenumber and forcing frequency (Table 2). In addition to these two main simulations, two others were conducted at each latitude, with half and double the forcing amplitude.

Results

Low-latitude: base case (Run LL1)

Despite the simple form of the forcing functions, a relatively complex wavefield quickly emerges. Figure 1 shows snapshots from Run LL1 after a couple days and nearly a month. The early snapshot of horizontal velocity shows a simple pattern of upwardly propagating waves (upper left panel). Because no appreciable energy has yet been transferred to high wavenumbers, the dissipation rate is negligible (upper middle panel). Spectra confirm that energy is tightly banded around the forcing wavenumbers and tidal frequency (right panels, thick grey). In the later snapshot energy has spread out to a wide range of scales and frequencies. Remarkably, there is no significant peak at the forcing (tidal) frequency in the later snapshot, but a large peak can be seen near the inertial frequency. Low-frequency (low aspect ratio) motions are visible as banded structures of horizontal velocity in the later snapshot (lower left). The dissipation

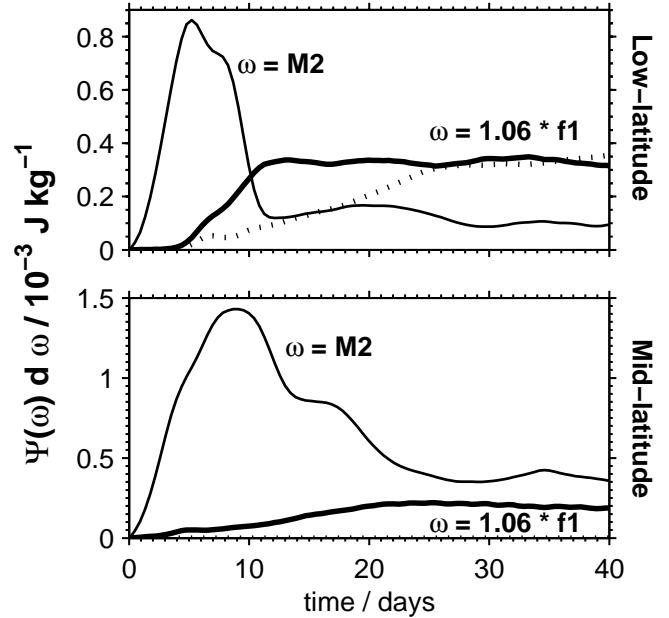


Figure 2. Integrated spectral energy in two frequency bands, $\Sigma\Psi(\omega)d\omega$, of width $d\omega = 1.4 \times 10^{-5} \text{ s}^{-1}$ centered at $\omega = 5.6 \times 10^{-5} \text{ s}^{-1}$ and $\omega = 1.4 \times 10^{-4} \text{ s}^{-1}$ (thick and thin solid lines). The frequency spectra, $\Psi(\omega, t)$ were calculated at each time from wavenumber spectra using the linear dispersion relationship. The lower frequency band includes both inertial and near-inertial motions; to separate these dynamically different processes, motions in this frequency band with non-zero horizontal wavenumber (super inertial, thick solid line), and zero horizontal wavenumber (inertial, dotted line) are plotted separately.

rate is patchy, as observations often suggest, with elevated regions visible near the bands of strong velocity (and strong shear). The patterns and typical scales of velocity and dissipation rate fluctuations are qualitatively similar to observed data [Polzin 2003a].

The transition from dominantly tidal (in a depth-averaged sense) to lower frequency motions occurs rapidly and early on in the simulation (Fig. 2). During the first few days, the newly generated internal tide is largely in phase with the forcing, and we see a rapid rise in tidal energy. After five days the first waves have reflected off the top bound-

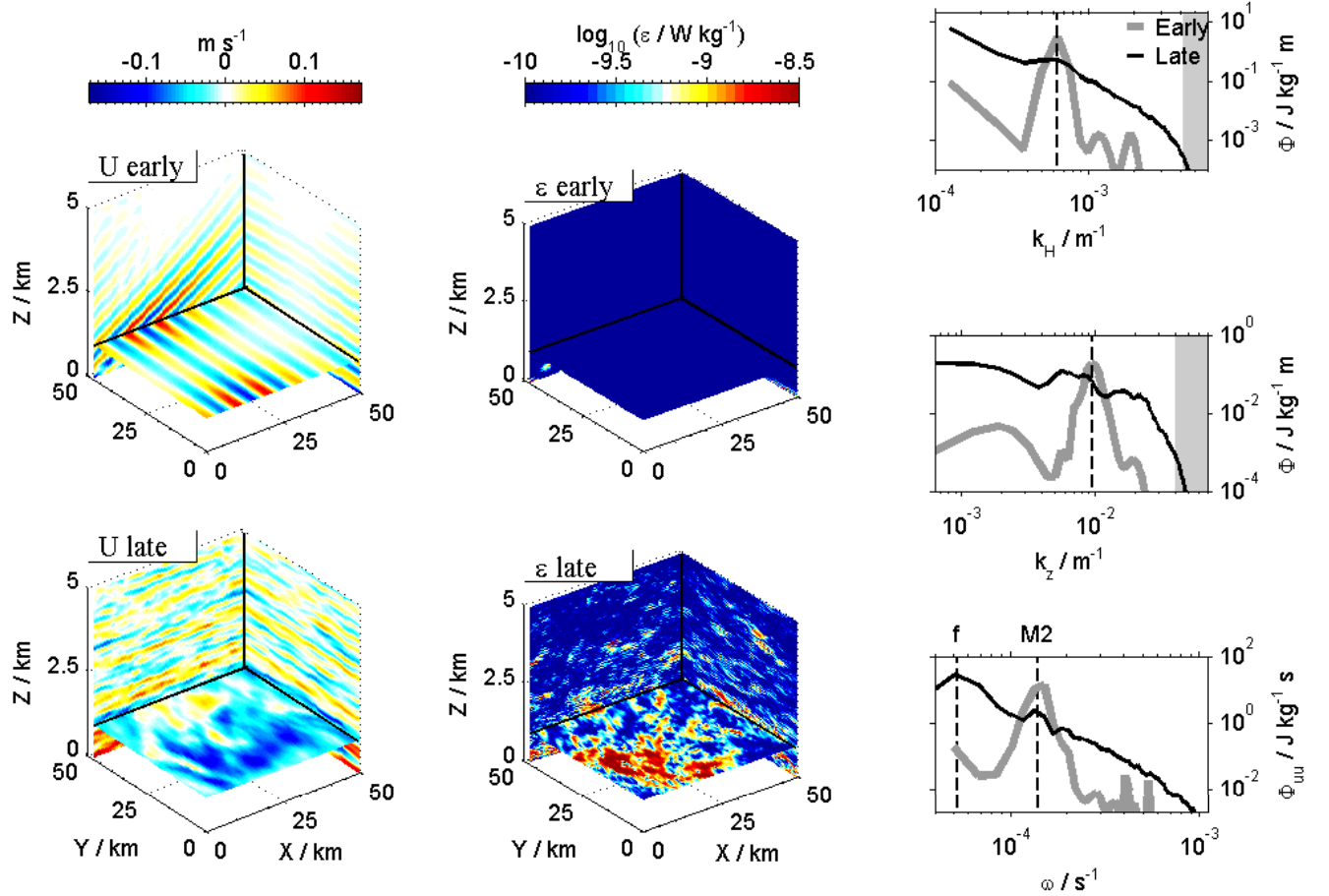


Figure 1. Left panels: slices of eastward horizontal velocity after 2 days (4 forcing periods) and 43 days (82 forcing periods) from the low-latitude simulation (Run LL1). Slices are located 2.5 km horizontally and 1 km vertically away from the domain boundaries. Middle panels: dissipation rate (2) at these times. Right panels: early (thick, grey) and late (thin, black) depth-averaged power spectra of horizontal kinetic energy as a function of horizontal wavenumber ($k_h = |(k_x, k_y)|$), vertical wavenumber (k_z), and frequency. Frequency spectra for the early snapshot was calculated from wavenumber spectra using the linear dispersion relationship, while frequency spectra for the later time is based on a 4-day time series. Central forcing frequencies/wavenumbers are indicated with vertical dotted lines. Grey shaded regions indicate wavenumber ranges in which hyperviscosity acts to damp motion in less than a day.

Table 2. Run parameters, from left to right: run label, forcing amplitude, local inertial frequency, forcing vertical wavenumber, depth-averaged total energy averaged over days 20-40, average energy from super-inertial motions only, and average dissipation rate. Depth averages taken only above the forcing region ($z \geq 0.8km$).

Run	A_0 / m	f / s^{-1}	k_{z0} / m^{-1}	\bar{E}_{tot} / Jkg^{-1}	$\bar{E}_{waves} / Jkg^{-1}$	$\bar{\epsilon} / Wkg^{-1}$
LL1	1.0	-5.3×10^{-5}	9.6×10^{-3}	1.1×10^{-3}	6.9×10^{-4}	2.9×10^{-10}
LL2	2.0	-5.3×10^{-5}	9.6×10^{-3}	2.1×10^{-3}	1.5×10^{-3}	1.1×10^{-9}
LL3	0.5	-5.3×10^{-5}	9.6×10^{-3}	5.5×10^{-4}	5.0×10^{-4}	1.9×10^{-10}
ML1	1.0	-1×10^{-4}	1.3×10^{-2}	1.1×10^{-3}	1.1×10^{-3}	5.9×10^{-10}
ML2	2.0	-1×10^{-4}	1.3×10^{-2}	1.9×10^{-3}	1.9×10^{-3}	1.4×10^{-9}
ML3	0.5	-1×10^{-4}	1.3×10^{-2}	1.9×10^{-2}	8.4×10^{-3}	1.4×10^{-10}

ary and begun to propagate downwards (not shown). Over the next few days there is a rapid redistribution of energy to other wavenumbers and frequencies, and, as a result, a loss of coherence between the wavefield and the forcing. Most of the transition between the narrow and broad spectral shapes shown in Figure 1 occurs during this period. In particular, the tidal energy declines while near-inertial energy rises. After approximately 10 days, the wavefield becomes steady in the sense that tidal and near-inertial wave energies stabilize with a ratio close to 1:3. However, energy slowly accumulates in inertial and sub-inertial motions with zero horizontal wavenumber throughout and several months beyond the period shown here (Fig. 2, dotted line).

Two-dimensional spectra of horizontal velocity provide further insight into the distribution of waves present in the quasi-steady state (Fig. 3, left). Two major features are apparent. First, the peak in energy at the forcing frequency and wavenumber is small. Instead there is an accumulation of energy near the inertial frequency at vertical wavenumbers ranging from half to several times the forcing wavenumber. Second, there is a band of energy centered below the forcing wavenumber extending out to high frequencies.

After about 10 days, when the magnitude and spectral properties of super-inertial motions have stabilized, average wave energy and dissipation rate both steadily decrease with height above the forcing region (bottom 800 m, Fig. 4). Inertial and sub-inertial energy (thick grey, left panel) also decreases steadily with height, though less smoothly. The conversion of depth-averaged tidal to near-inertial energy from Figure 2 is mirrored in the depth-evolution of frequency spectra (Fig. 4, right panel). At three increasing heights above the bottom, the tidal peak shrinks, while lower-frequency energy rises. Though depth-average energy spectra show a broad peak near and above the inertial frequency (Fig. 1), the spectrum from highest above bottom here is instead peaked at half the forcing frequency (Fig. 4, right panel, blue line).

Mid-latitude: base case (Run ML1)

At mid-latitude (Run ML1), most wave energy remains near the forcing frequency. The initial snapshots and spectra are similar to the low latitude case (Fig. 5). The flow evolution however, is significantly different. The final state shows neither the dominant near-inertial peak nor the associated banded structures in velocity. As with Run LL1, the initial rapid growth of tidal energy levels off after a few days (Fig. 2, bottom panel). In this case energy again appears at near-inertial frequencies but does not surpass that in the tidal band. There is no appreciable energy accumulation in inertial or sub-inertial motions. Unlike the low-latitude case, the average energy input from forcing and loss to dissipation are comparable; the system has achieved a truer steady state.

At this latitude, energy does not build up in near-inertial and inertial motions, but instead remains clustered near the forcing frequency and wavenumber (Fig. 3, right panel). As in the low-latitude case, there is a band of energy centered near half the forcing wavenumber spread through a wide range of frequencies. There are also patches of elevated energy at harmonics of the forcing frequency.

In steady-state, the mid-latitude waves maintain a dominantly tidal frequency, with steadily decreasing magnitude with height (Fig. 6). In contrast to the low-latitude case, here energy and dissipation rate rapidly decrease with height and level off a kilometer above the forcing region.

Varying amplitude

We now briefly consider the effect of changing the forcing amplitude at each latitude (Runs LL2, LL3, ML2, ML3, Table 2). As the low-latitude forcing amplitude is doubled, and doubled again, the saturation energy level also doubles twice (Table 2). With increasing amplitude the wave-field shear is distributed amongst a larger range of vertical scales (Fig. 7, top panel). In particular, with higher total spectral level there is an increasing spread of variance to lower wavenumbers. It is interesting to note (but beyond our cur-

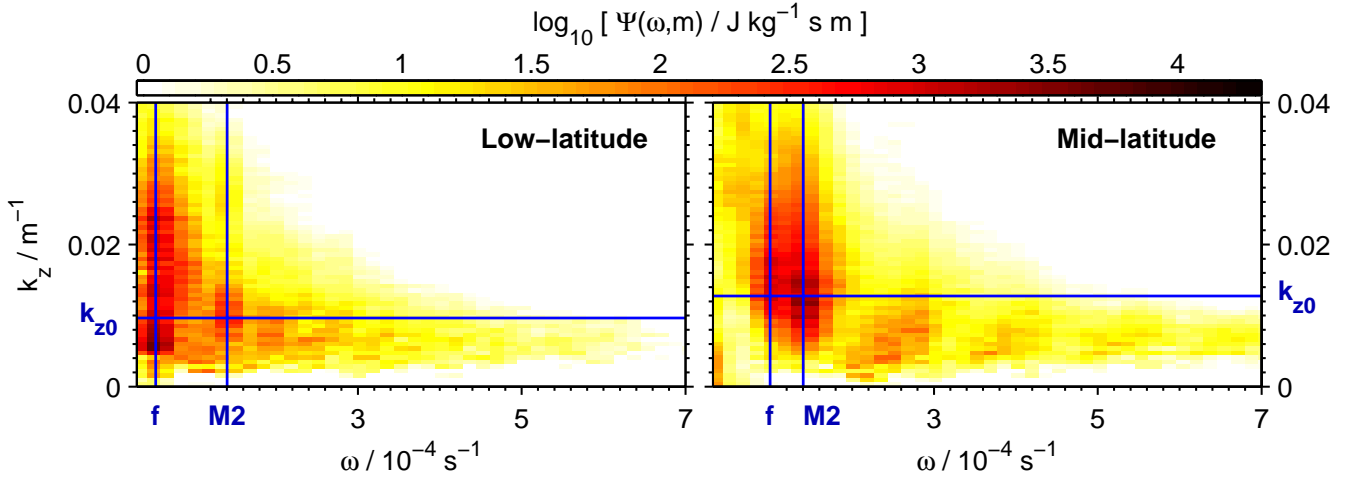


Figure 3. Two-dimensional spectra of eastward horizontal velocity as a function of frequency and vertical wavenumber for the base cases at low latitude (Run LL1, left) and mid latitude (Run ML1, right). Spectra were calculated from four day long time series starting 38 days into the run, and have been averaged over all horizontal wavenumbers. Blue lines indicate the tidal forcing frequency and local inertial frequency (vertical lines) and forcing wavenumber (horizontal lines).

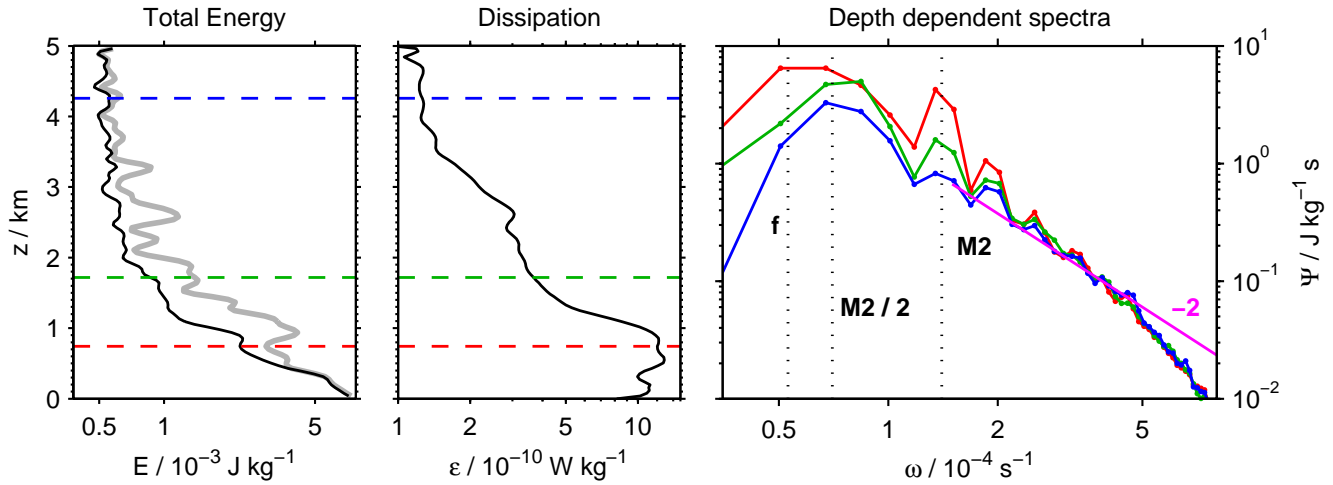


Figure 4. Left panel: Total energy (kinetic plus potential) averaged horizontally and over 4 days after the low-latitude simulation (Run LL1) has achieved a near-steady state. Thin black and thick grey lines represent data with non-zero horizontal wavenumber (super-inertial) and zero-horizontal wavenumber (inertial and sub-inertial) respectively. Middle panel: average dissipation rate over this period. Right panel: horizontal kinetic energy frequency spectra calculated from time series at three depths as indicated by horizontal dashed lines in the left and middle panels. Vertical dashed lines indicate the forcing frequency (M2), half the forcing frequency, and the inertial frequency. A line with a -2 slope is shown for reference.

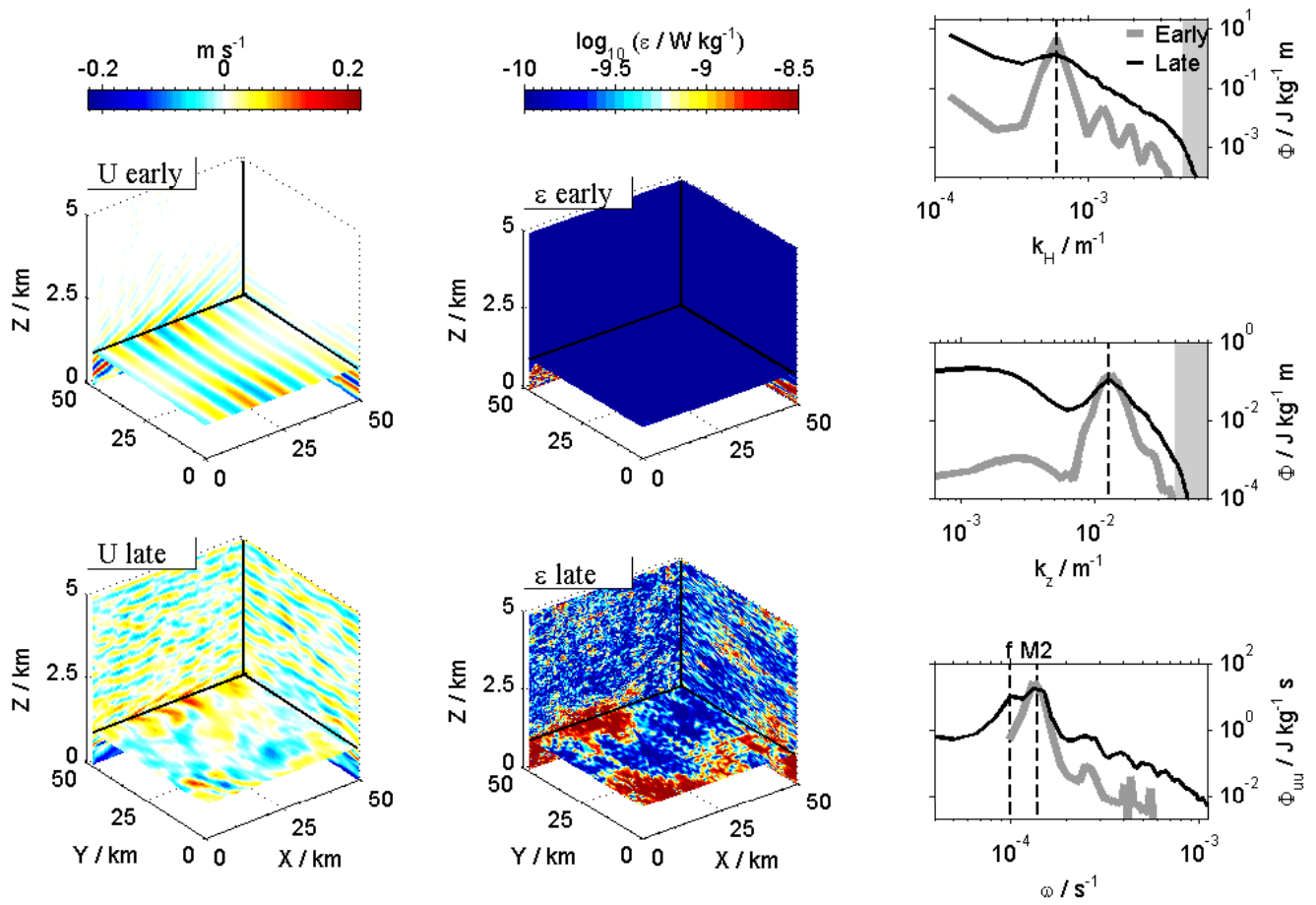


Figure 5. Same as Fig. 1, for mid-latitude (Run ML1).

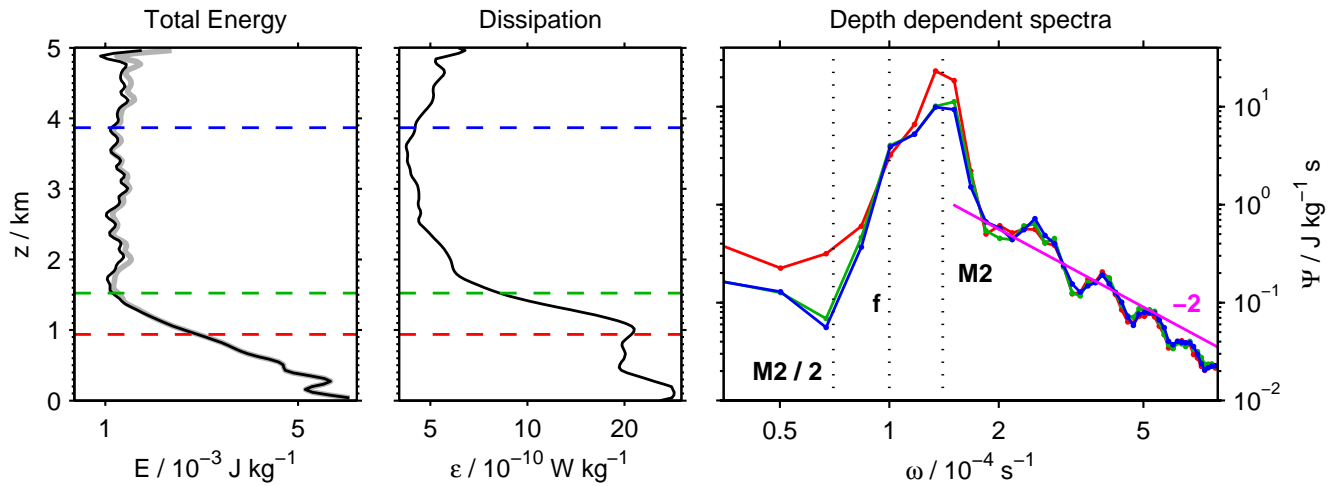


Figure 6. Same as Fig. 4 for mid-latitude (Run 2).

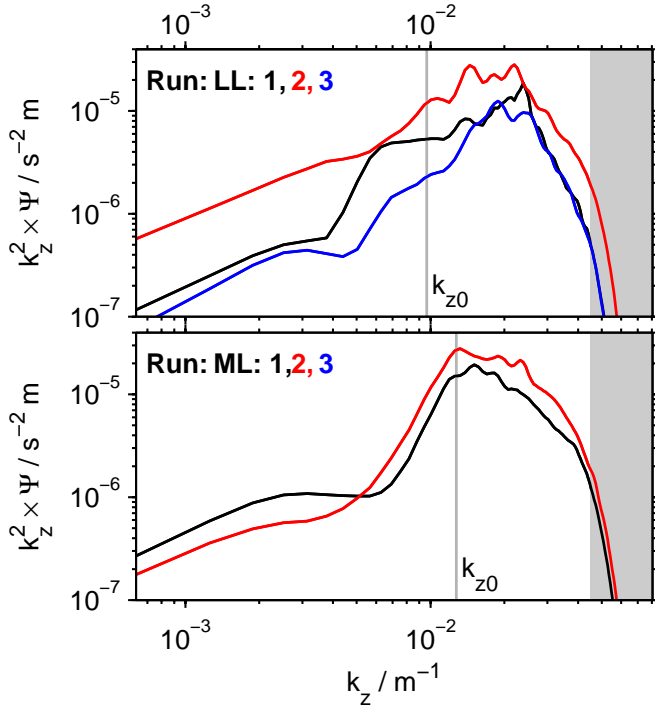


Figure 7. Shear spectra for low-latitude (top) and mid-latitude (bottom) simulations. The forcing wavenumber (Table 2) at each latitude is indicated with a vertical grey line. Grey shaded regions indicate wavenumber ranges in which hyperviscosity acts to damp motion in less than a day.

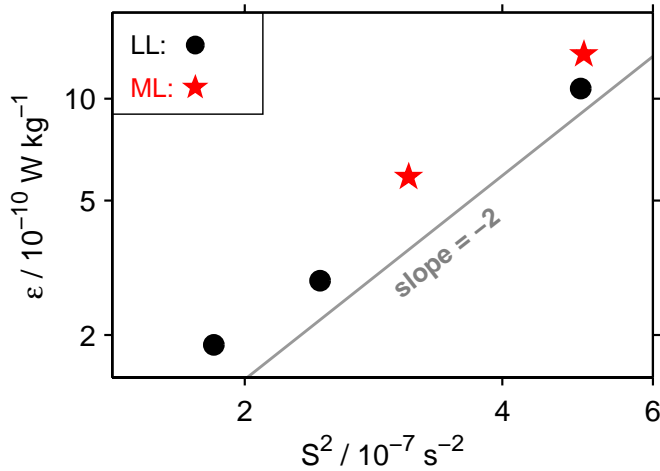


Figure 8. Integrated shear spectra (Fig. 7) versus the average dissipation rate above the forcing region ($z \geq 0.8\text{km}$) for low-latitude (black circles) and mid-latitude (red stars) simulations. A -2 slope is shown for reference.

rent ability to understand) that all three spectra are peaked at or just above twice the forcing wavenumber. At mid-latitude, shear spectra are peaked at the forcing wavenumber, with variance primarily spread to higher wavenumbers. Compared to the low-latitude cases, mid-latitude shear spectra maintain consistent shape with varying amplitude (Fig. 7, right panel). Integrated shear variance has a strong relationship with average dissipation rate amongst all simulations (Fig. 8).

Discussion

Wave-wave interactions and spectral evolution

Energy may be transferred between finite amplitude internal waves through the nonlinear terms in (1). Though in general the transfer rates are complicated and somewhat impenetrable, *McComas and Bretherton* [1977] argued that for spectral distributions similar to the , energy transfer is dominated by a few classes of interactions that can be described in relatively simple terms. One of these is Parametric Subharmonic Instability (PSI), which involves the transfer of energy from an energetic initial wave to waves of smaller vertical scale and half the frequency. PSI is a candidate mechanism to transfer energy away from tidally forced waves only when the tidal frequency is at least twice the inertial frequency - a criteria that is met only for the low-latitude runs. Previous studies of PSI in GM-like wavefields have mitigated its importance by noting the relatively long associated timescales of interaction - typically on the order of tens of days for the vertical wavenumbers considered here [*McComas and Muller* 1977].

It is tempting to conclude that the apparently much more efficient transfer of energy out of the forcing bandwidth in the low latitude case is due to PSI, particularly given the spectral peaks at half the forcing frequency in Figure 4. However, a few caveats must be noted. First, energy appears at a range of vertical wavenumbers in the lower, near-inertial frequency band, many of which are actually smaller than the forcing wavenumber. Second, resonant wave interaction models are based upon statistical averages of randomly phased waves with prescribed spectral shapes. Comparisons with interaction timescales or other model features may not be appropriate for the bandwidth limited, coherently forced waves described here. In fact, both the initial wavefield evolution (Fig. 2) and the saturation spectral shapes (Figs. 4, 3) suggest that the transfer of energy out of the forcing frequency band is quite rapid.

Other features of the spectral evolution or final state observed here are even less easily explicable in terms of commonly discussed classes of wave-wave interaction. In particular, there is no previously described mechanism that we are aware of that operates to transfer energy to higher frequencies at low wavenumbers, a feature observed at both latitudes

(Fig. 3). We caution against overly strict comparison with any single mechanism - it is likely that the evolution here comes from a full array of resonant and off-resonant wave interactions.

Energy and dissipation

Over the last 30 years several studies have identified the dissipation rate with the modeled spectral transfer of energy from large (vertical) scale to small scale waves through wave-wave interaction (e.g. *Gregg et al* [2003], *Polzin et al* [1995], *Muller et al* [1986]). Several robust features of this family of predictions have been validated by a wide range of observational [*Gregg* 1989, *Polzin et al* 1995] and numerical [*Winters and D'Asaro* 1997] results, though few validation attempts have taken place near regions of energetic internal wave generation. Here we briefly consider several such features.

First, the average dissipation rate generally scales quadratically with wavefield amplitude. In the most recent formulations, amplitude is defined as a typical shear spectral level integrated over a range of vertical wavenumbers defined by a critical Richardson number criterion [*Gregg et al* 2003]. This method cannot be directly applied to our results, as the simulated waves succumb to hyperviscosity before the wave shear reaches the critical value. Furthermore, calculation of the spectral energy level in such methods is based on assumptions about the shape of vertical wavenumber spectra that are violated here (Fig. 7). Despite spectral differences, there is a strong, close to quadratic relationship between total shear variance and average dissipation rate for all six of the simulations presented here (Fig. 8). There is also a good correlation between average dissipation rate and both the total and super-inertial energy in each run (Table 2).

The second robust prediction to come from wave-wave interaction based models of turbulence is that the average dissipation rate should increase with latitude. The explanation, as described by *Gregg et al* [2003], is that the dissipation rate depends on a characteristic wavefield aspect ratio, or equivalently a characteristic frequency. For near-inertially dominated (GM) wavefields, the energy containing frequency increases with latitude. In the lower water column, the mid-latitude dissipation rate is approximately twice as large as the average low-latitude dissipation rate in a comparably strong wavefield (Figs. 4, 6). In fact, the elevated lower water-column dissipation is comparatively larger than than the correction factor ($L(\theta)$) of *Gregg et al*. This elevation may be related to the fact that the average energy-containing frequency in our mid-latitude simulation is closer to tidal than inertial (Fig. 6, Table 2). However, as the mid-latitude dissipation rate decreases more quickly with height above bottom, the depth-averaged dissipation rates are only slightly larger at the higher latitude (Fig. 8).

There are significantly fewer theories addressing the ver-

tical structure of dissipation near generation regions. Observed profiles of energy and dissipation over rough topography in in the Brazil Basin both decline significantly within 500 meters above bottom [*Polzin et al* 1997]. *Polzin* [2003a] propose a kinematic model in which the steady-state energy level at each height is set by a balance between dissipation, itself a quadratic function of energy, and vertical energy flux divergence. In all of our simulations the average dissipation rate declines with height, though not quite as quickly as in the observations or *Polzin's* model. We suspect that the relatively large decay scale of simulated low-latitude dissipation reflects the choice of a moderately sized forcing wavenumber. Direct forcing of high-wavenumber waves could lead to enhanced near-bottom dissipation. Topographic scattering of downwardly propagating low-mode waves may also lead to bottom-intensified turbulence [*St. Laurent and Garrett* 2002, *Muller and Xu* 1992] but is not included in these simulations.

Conclusions

We have presented results from simulations of nonlinearly evolving internal wave fields at representative low and mid latitudes. All cases were forced with a simple bottom-localized, narrowband upwardly propagating internal tide, yet all quickly spread energy to a variety of scales and frequencies. In the low-latitude simulations, depth-averaged energy was quickly transferred out of the M2 frequency band into inertial and near-inertial motions. After about 10 days the wavefield became steady in the sense that the magnitude and spectral characteristics of super-inertial energy stabilized. In this state energy spectra evolved from tidally to dominated to have significant spectral peaks between half the tidal (forcing) frequency and the local inertial frequency. Average super-inertial energy and dissipation both declined steadily with height. The saturation energy level increased linearly with changes in forcing amplitude. For increasing wave energy / spectral level, vertical wavenumber spectra became increasingly broad, and the average dissipation rate grew quadratically.

At mid-latitude, wave energy remained significantly more localized around the forcing frequency and vertical wavenumber. The saturation wavefield maintained a steady spectral shape and smoothly declined in amplitude with increasing height above bottom. The average dissipation rate was larger in the lower water column than that at low-latitude (for similar wavefield energy), but declined more quickly with height.

Overall we find these results to be very encouraging. Given the simple form of the forcing, the fact that the saturation states selected by internal dynamics display spectral properties and kinematic relationships similar to ocean observations and theoretical predictions is remarkable. In particular, it suggests that the important dynamics are relatively robust and are captured by the scales resolved here. We con-

clude that similar methods hold great promise for further exploration of mixing above rough topography as well as a host of other energetic internal-wave regimes. Hopefully such work will be instrumental in the development of global models of internal-wave generation, propagation, and decay (e.g. Alford [this issue], and Muller [this issue]).

Acknowledgments. This work brought to you by NSF (OCE 0242471) and ONR (N0014-96-1-0616). We continually benefit from discussions with colleagues working on all aspects of the ‘internal waves: birth to death’ problem. I was delighted to be invited to AHA, and am indebted to the conveners for organizing such a productive and enjoyable workshop.

References

- Egbert, G.D. and R.D. Ray, Significant dissipation of tidal energy in the deep ocean inferred from satellite altimeter data, *Nature*, 405, 775–778, 2000.
- Garrett, C.J.R. and W.H. Munk, Space-timescales of internal waves, *Geophys. Fluid Dynamics*, 2, 225–264, 1972.
- Gregg, M.C. and T.B. Sanford and D.P. Winkel, Reduced mixing from the breaking of internal waves in equatorial waters, *Nature*, 422, 513–515, 2003.
- Gregg, M.C., Scaling turbulent dissipation in the thermocline, *J. Geophys. Res.*, 94, 9686–9698, 1989.
- Hasumi, H. and N. Sugimotohara, Effects of locally enhanced vertical diffusivity over rough bathymetry on the world ocean circulation, *J. Geophys. Res.*, 104, 23,637–23,374, 1999.
- Heney, F.S., J. Wright, and S.M. Flatte, Energy and action flow through the internal wave field: An eikonal approach, *J. Geophys. Res.*, 91, 8487–8495, 1986.
- Ledwell, J.R. and A.J. Watson and C.S. Law, Evidence for slow mixing across the pycnocline from an open-ocean tracer release experiment, *Nature* 364, 701–703, 1993.
- Ledwell, J.R. and E.T. Montgomery and K.L. Polzin and L.C. St. Laurent and R.W. Schmitt and J.M. Toole, Evidence for enhanced mixing over rough topography in the abyssal ocean, *Nature*, 403, 179–182, 2000.
- Llewellyn Smith, S.G. and W.R. Young, Conversion of the barotropic tide, *J. Phys. Oceanogr.*, 32, 1554–1566, 2002.
- McComas, C.H. and P. Muller, Timescales of resonant interactions among oceanic internal waves, *J. Phys. Oceanogr.*, 11, 139–147, 1981.
- Muller, P., and N. Xu, Scattering of oceanic internal waves off random bottom topography, *J. Phys Oceanogr.*, 22, 474–488, 1992.
- Munk, W., Abyssal Recipes, *Deep-Sea Res.*, 13, 707–730, 1966.
- Polzin, K., J.M. Toole and R.W. Schmitt, Finescale parameterization of turbulent dissipation, *J. Phys Oceanogr.*, 25, 306–328, 1995.
- Polzin, K., Idealized solutions for the energy balance of the finescale internal wavefield, *J. Phys Oceanogr.*, in press, 2003.
- Polzin, K., Notes on the internal wave spectrum, *J. Phys Oceanogr.*, in press, 2003.
- Polzin, K., J.M. Toole, J.R. Ledwell and R.W. Schmitt, Spatial variability of turbulent mixing in the abyssal ocean, *Science*, 276, 93–96, 1997.
- St. Laurent, L. and C. Garrett, The role of internal tides in mixing the deep ocean, *J. Phys. Oceanogr.*, 32, 2882–2899, 2002.
- Simmons, H.L., S.R. Jayne, L.C. St. Laurent, and A.J. Weaver, Tidally driven mixing in a numerical model of the ocean general circulation, *Ocean Modelling*, in press, 2003.
- Slinn, D.N. and J.J. Riley, A model for the simulation of turbulent boundary layers in an incompressible stratified flow, *J. Comput. Phys.*, 144, 550–602, 1998.
- Winters, K.B. and E.A. D’Asaro, Direct simulation of internal wave energy transfer, *J. Phys. Oceanogr.*, 27, 1937–1945, 1997.
- Winters, K.B. and J.A. MacKinnon and B. Mills, A spectral model for process studies of rotating, density-stratified flows, *submitted*, 2003.

This preprint was prepared with AGU’s \LaTeX macros v4, with the extension package ‘AGU++’ by P. W. Daly, version 1.6a from 1999/05/21.